Supplementary Information

Haoran Ma[1,2,3], J. Pedro F. Nunes[4], Ambar Banerjee[5], Martin Centurion[6], Kareem Hegazy[11], Renkai Li[7], Yusong Liu[8], Xiaozhe Shen[9, 10], Xijie Wang[9], Stephen Weathersby[9], Philippe Wernet[5], Thomas J. A. Wolf[8], Michael Odelius[12*], Jie Yang[1*]

[1*]Center of Basic Molecular Science, Department of Chemistry, Tsinghua University, Beijing, 100084, China.
[2]Zhili College, Tsinghua University, Beijing, 100084, China.
[3]Department of Physics, Stanford University, Stanford, 94305, CA, United States of America.
[4]Diamond Light Source Ltd, Didcot, OX11 0DE, United Kingdom.
[5]Department of Physics and Astronomy, Uppsala University, Uppsala, Sweden.
[6]Department of Physics and Astronomy, University of Nebraska–Lincoln, Lincoln, 68588, NE, United States of America.
[7]Department of Engineering Physics, Tsinghua University, Beijing, 100084, China.
[9]SLAC National Accelerator Laboratory, 2575 Sand Hill Road, Menlo Park, 94025, CA, United States of America.
[8]Stanford PULSE Institute, SLAC National Accelerator Laboratory, 2575 Sand Hill Road, Menlo Park, 94025, CA, United States of America.
[10]Institute of Advanced Science Facilities, Shenzhen, China.
[11]Department of Statistics, University of California Berkeley, 367 Evans Hall, Berkeley, 94720, CA, United States of America.
[12*]Department of Physics, Stockholm University, Stockholm, SE-106 91, Sweden.

*Corresponding author(s). E-mail(s): odelius@fysik.su.se; jieyang1@tsinghua.edu.cn;
Contributing authors: mahr@stanford.edu; pedro.nunes@diamond.ac.uk; ambar.banerjee@physics.uu.se; martin.centurion@unl.edu;

khegazy@berkeley.edu; lirk@tsinghua.edu.cn; yusongl@slac.stanford.edu;
shenxiaozhe@mail.iasf.ac.cn; wangxj@slac.stanford.edu;
spw@slac.stanford.edu; philippe.wernet@physics.uu.se;
thomas.wolf@slac.stanford.edu;

1 Determination of molecular diffraction from the experimental data

The comprehensive procedure transitioning from the radially integrated experimental signal ($I_{\text{tot}}(s)$) to the modified diffraction intensity ($sM(s)$) has been thoroughly elucidated in previous publications[1, 2]. In brief, $I_{\text{tot}}(s)$ comprises three distinct components: elastic molecular diffraction ($I_{\text{mol}}(s)$), elastic atomic diffraction ($I_{\text{at}}(s)$), and inelastic diffraction ($I_{\text{ine}}(s)$).

$$I_{tot}(s) = I_{mol}(s) + I_{at}(s) + I_{ine}(s) \tag{1}$$

The elastic molecular diffraction ($I_{\text{mol}}(s)$) segment encapsulates the majority of the structural details. Hence, it's advantageous to transform it into the modified diffraction intensity ($sM(s)$):

$$sM(s) = s\frac{I_{mol}(s)}{I_{at}(s)} \tag{2}$$

$I_{at}(s)$ could be easily calculated through the elastic atom scattering factors.

To extract the static $I_{\text{mol}}(s)$ from the static $I_{\text{tot}}(s)$ (acquired with delay-stage points before time zero), we employ the zero points (s_0) derived from the elastic molecular diffraction of the AIMD simulated ambient temperature structure (referenced below). At these specific points, we assume that the contribution of $I_{\text{mol}}(s_0)$ to $I_{\text{tot}}(s_0)$ is negligible:

$$I_{tot}(s_0) = I_{at}(s_0) + I_{ine}(s_0) \tag{3}$$

Next, we fit these points with a weighted exponential function to obtain an estimation of the combined elastic atomic diffraction and inelastic diffraction. Subtracting this fitted curve from the integrated experimental signal yields the static $I_{\text{mol}}(s)$.

For dynamic signals, we operate under the assumption that the elastic atomic diffraction and inelastic diffraction remain unchanged throughout the reaction. Hence, the calculation of the modified diffraction intensity difference ($\Delta\text{sM}(\text{s}, \text{t})$) is as follows:

$$\Delta\text{sM}(\text{s}, \text{t}) = s\frac{I_{tot}(s,t) - I_{tot}(s,t_0)}{I_{at}(s)} \tag{4}$$

An artificial baseline emerges due to the normalization of each individual image. To address this, second-order polynomials are utilized to fit and subsequently remove this baseline from each image's corresponding ΔsM. Subsequently, the ΔsMs are averaged at each delay-stage position. Gaussian smoothing is applied to both the s axis (with

a full width at half maximum of 0.2Å^{-1}) and the t axis (with a full width at half maximum of 150 fs).

Furthermore, the signal within the 0 < s < 0.6Å range is lost due to the presence of a hole in the middle of the phosphor screen. To mitigate this loss, a sine function extrapolation is employed to smoothly compensate for it.

2 Determination of molecular diffraction from the AIMD simulation

As discussed in the main text, the molecule exhibits significant vibrational motion, leading to a distribution of distances rather than precise values for each atom pair. The AIMD simulation provides pair distribution functions for each atom pair ($PDF_{ij}(r)$). Using the independent atom model (IAM), the elastic molecular diffraction can be calculated from these $PDF_{ij}(r)$.

$$I_{mol}(s) = \sum_i \sum_{j,j\neq i} \int_0^\infty PDF_{ij}(r)|f_i(s)| \cdot |f_j(s)| \frac{\sin(s \cdot r)}{s \cdot r} \mathrm{d}r \tag{5}$$

The elastic scattering factors of atoms, $f_i(s)$, are calculated using the ELSEPA program[3]. The modified diffraction intensity($sM(s)$) is calculated by Eqn.2.

3 Determination of pair distribution functions (PDF)

The calculation of pair distribution functions ($PDF(r)$) from $sM(s)$ essentially involves the inverse transformation of the equation mentioned in the text (Eqn. 5), irrespective of the specific types of atom pairs involved, which are valued by their respective scattering factors.

$$PDF(r) = \int_0^{s_{max}} sM(s) sin(s \cdot r) e^{-s^2/k^2} \mathrm{d}s \tag{6}$$

Additionally, a Gaussian filter is applied to dampen noise at high s values. When calculating the static $PDF(r)$, a parameter k is set to 6.3Å^{-1}.

4 Determination of pair distribution function difference on parallel(ΔPDF$_\parallel$) and perpendicular(ΔPDF$_\perp$) directions from the experimental data

The intricate process of anisotropic analysis of electron diffraction data has been elaborated elsewhere[4, 5]. Essentially, a linearly polarized laser generates an ensemble of excited molecules with cylindrical symmetry, resulting in a three-dimensional cylindrical symmetric pair distribution function. Subsequently, the electron beam is diffracted by the projected pair distribution function along the beam direction and

interferes on the detector, producing an anisotropic diffraction pattern. Therefore, the data analysis involves an inverse process: initially reconstructing the projected pair distribution function using inverse Fourier transform, followed by reconstructing the original cylindrical symmetric pair distribution function using inverse Abel transform.

To delve into specifics, the initial step involves normalizing the diffraction pattern using isotropic 2-D atomic diffraction I_{at}, accentuating the detailed structure from the decaying signal along momentum transfer. Subsequently, the image is partitioned into four parts by two axes: the polarization direction of the laser and another direction perpendicular to it, centered at the electron beam's position. If the anisotropy stems solely from one-photon excitation, ideally, these four quarters should exhibit a $\cos^2\theta$ distribution. Thus, ideally, these quarters should be equivalent. They are then averaged to mitigate noise. Next, a Legendre fitting is employed to extract the coefficients of the 0th and 2nd order Legendre polynomials (β_0 and β_2, corresponding to the isotropic term and the $\cos^2\theta$ distribution term)[6].

$$I(s,\theta) = \sum_{l=0}^{\infty} \beta_l(s) P_l(\cos(\theta)) \tag{7}$$

After retrieving the diffraction pattern using Eqn. 7 with only β_0 and β_2, we apply a 2-D fast Fourier transform (2-D FFT) and inverse Abel transform using the r-basex algorithm. This process yields a slice of the 3-D cylindrical symmetric pair distribution function. The average of $0° \sim 10°$ and $80° \sim 90°$ corresponds to the parallel ($\Delta\text{PDF}_{\parallel}$) and perpendicular ($\Delta\text{PDF}_{\perp}$) pair distribution function differences, respectively.

5 Determination of pair distribution function difference on parallel($\Delta\text{PDF}_{\parallel}$) and perpendicular($\Delta\text{PDF}_{\perp}$) directions from the AIMD simulation

The diffraction pattern resulting from an oriented molecule ensemble induced by one-photon excitation can be calculated using Eqn. 8[7, 8]:

$$I(s,\theta) = \sum_i \sum_{j,j\neq i} 3|f_i(s)| \cdot |f_j(s)| \{ \frac{j_1(sr_{ij})}{sr_{ij}} - [\sin^2\Omega_{ij} + (2 - 3\sin^2\Omega_{ij})\cos^2\theta] \frac{j_2(sr_{ij})}{2} \} \tag{8}$$

In this equation, j_1 and j_2 represent the first order and second order spherical Bessel functions, respectively. Ω_{ij} denotes the angle between atom pair ij and the transition dipole moment μ, while θ indicates the angle relative to the direction of polarization on the detector.

Subsequently, the diffraction patterns of each trajectory at each time point are averaged and processed using the same method as described in section 4 to obtain $\Delta\text{PDF}_{\parallel}$ and $\Delta\text{PDF}_{\perp}$.

6 Determination of uncertainty using bootstrap algorithm

For all the functions mentioned above, we follow a bootstrap procedure for uncertainty estimation[1, 4]. Initially, we randomly select two-third of the individual data, such as 60 images out of 90 at each delay stage point or 80 trajectories out of 120 from the AIMD simulation. Subsequently, using this subset of data and the same methodology, we calculate the target function. This process is then iterated 1000 times. The standard deviation of the results from these 1000 iterations provides the uncertainty measure.

7 Estimation of the excitation ratio

To determine the excitation ratio, we first calculate the ratio S, which is the absolute value of the integrated experimental molecular diffraction signal to the integrated simulated signal within the range of $2.1 \sim 6.2\,\text{Å}^{-1}$. Next, we compute T, the ratio of the integrated molecular diffraction difference within the $0.5 \sim 1\,\text{Å}^{-1}$ range, comparing the average experimental signal from 0.5 to 1 ps with the AIMD simulation of $Fe(CO)_4$. The excitation ratio is then obtained as T/S, where S scales the transient experimental signal into simulation units, and dividing by the simulated signal level corresponding to 100% excitation yields an excitation ratio of 13.2%.

8 Determination of anisotropic parameter η

η is defined by the following equation:

$$\eta(r) = \frac{\Delta\text{PDF}_{\parallel}(\text{r}) - \Delta\text{PDF}_{\perp}(\text{r})}{|\Delta\text{PDF}_{\parallel}(\text{r})| + |\Delta\text{PDF}_{\perp}(\text{r})|} \tag{9}$$

All the η values shown in the main text are the averages of $\eta(r)$ between $r = 2.8$Å and 3.2Å. The η values for pure axial and pure equatorial dissociation are calculated using the $\Delta\text{PDF}_{\parallel}(\text{r})$ and $\Delta\text{PDF}_{\perp}(\text{r})$, from the simple removal of axial or equatorial CO from $Fe(CO)_5$, respectively. The random dissociation value is calculated by $\Delta\text{PDF}_{\parallel}(\text{r})$ and $\Delta\text{PDF}_{\perp}(\text{r})$ from an ensemble composed of half pure axial and half pure equatorial dissociation described above.

9 Determination of dynamic parameters using genetic fitting

In genetic fitting process employing the PyGad module[9], the fitting parameters are configured as follows:

```
num_generations = 1000
num_parents_mating = 512
sol_per_pop = 512
parent_selection_type = "sss"
keep_parents = 256
```

```
crossover_type = "single_point"
crossover_probability=0.6
mutation_type = "random"
mutation_probability = 0.6
```

And the fitness is calculated using eqn.10

$$Fitness = 1/\int (\frac{F_{\text{expt}}(x) - F_{\text{sim}}(x)}{\sigma_{\text{expt}}(x)})^2 \text{dx} \tag{10}$$

In this equation, F_{expt} represents the experimental data awaiting fitting, while σ_{expt} denotes its corresponding uncertainty. F_{sim} represents the function generated by the dynamic parameters during the fitting process.

9.1 Kinetic parameters of the sequential dissociation

Here $F_{\text{expt}}(t)$ represents the integration of $\Delta\text{sM}(s,t)$ between $0.5\text{Å}^{-1} < \text{s} < 1\text{Å}^{-1}$, normalized by the average of the last two points ($t = 30$ps and $t = 50$ps). We introduce three parameters: the start of dissociation t_0, the time constant of the first dissociation τ_1, and the time constant of the second dissociation τ_2.

$$F_{sim}(t) = \begin{cases} 0, & t < t_0 \\ A(e^{-\frac{t-t_0}{\tau_1}} - 1) + (1-A)(1 - e^{-\frac{t-t_0}{\tau_1}})(e^{-\frac{t}{\tau_2}} - 1), & t \geq t_0 \end{cases} \tag{11}$$

In this equation, A represents the ratio of the integration of $\Delta\text{sM}(s,t)$ in the range $0.5\text{Å}^{-1} < \text{s} < 1\text{Å}^{-1}$ between AIMD simulated $Fe(CO)_4$ and $Fe(CO)_3$.

9.2 Structural parameters at the pre-dissociation area

As discussed in the main text, the vibration of the excited molecule is substantial. Consequently, the distance between atom pair ij ceases to be an exact value. To compute the diffraction pattern from its structural parameters, Eqn. 8 needs to be modified to resemble the form of Eqn. 5.

$$I(s,\theta) = \sum_{ij} 3|f_i|\cdot|f_j| \int_0^\infty PDF_{ij}(r)\{\frac{j_1(sr)}{sr} - [\sin^2\Omega_{ij} + (2 - 3\sin^2\Omega_{ij})\cos^2\theta]\frac{j_2(sr)}{2}\}\text{dr} \tag{12}$$

If we presume that the vibration is harmonic, meaning its pair distribution function assumes a Gaussian shape, and as long as the vibration is not excessively strong ($\sigma \leq 0.5\text{Å}$), equation 12 can be simplified as follows:

$$I(s,\theta) = \sum_{ij} 3|f_i| \cdot |f_j|\{\frac{j_1(sr)}{sr} - [\sin^2\Omega_{ij} + (2 - 3\sin^2\Omega_{ij})\cos^2\theta]\frac{j_2(sr)}{2}\}e^{\frac{-l^2s^2}{2}} \tag{13}$$

In this equation, l represents the strength of the vibration, which corresponds to the standard deviation (σ) of its Gaussian-shaped pair distribution function.

In this approach, we adopt a separation of parameters: parameters that only affect the axial direction ($\Delta\mathrm{PDF}_{\parallel}$) and those that only affect the equatorial direction ($\Delta\mathrm{PDF}_{\perp}$). We assume that all $Fe(CO)_5$ molecules are in D_{3h} symmetry.

When fitting the axial direction, five parameters are introduced: the dissociation ratio, the axial Fe-C bond length of $Fe(CO)_5$, and the vibration strengths of axial Fe-C, axial-equatorial C-O, and axial-equatorial C-C atom pairs. The structure of $Fe(CO)_4$ is not considered during this fitting. Instead, when calculating the simulated $\Delta\mathrm{PDF}_{\parallel}$, the contribution of $Fe(CO)_4$ is represented by the average of the experimental $\Delta\mathrm{PDF}_{\parallel}$ between 0.8ps and 1.5ps.

In the equatorial direction, four parameters are introduced: the equatorial Fe-C bond length of $Fe(CO)_5$, and the vibration strengths of equatorial Fe-C, equatorial-equatorial C-O, and equatorial-equatorial C-C atom pairs. The dissociation ratio is manually set to 0, reflecting the absence of equatorial dissociation in the pre-dissociation area.

In each fitting iteration, $F_{\mathrm{expt}}(r)$ represents either $\Delta\mathrm{PDF}_{\parallel}$ or $\Delta\mathrm{PDF}_{\perp}$ at a specific time point, and $F_{\mathrm{sim}}(r)$ is its corresponding ΔPDF generated by the model described above and Eqn. 13.

The general fitting results, compared with experimental data, are presented in Fig. 1. Additionally, Fig. 2 illustrates the relationship between fitness and the number of generations across multiple fitting processes. The results confirm that the number of generations is sufficient for the algorithm to achieve convergence.

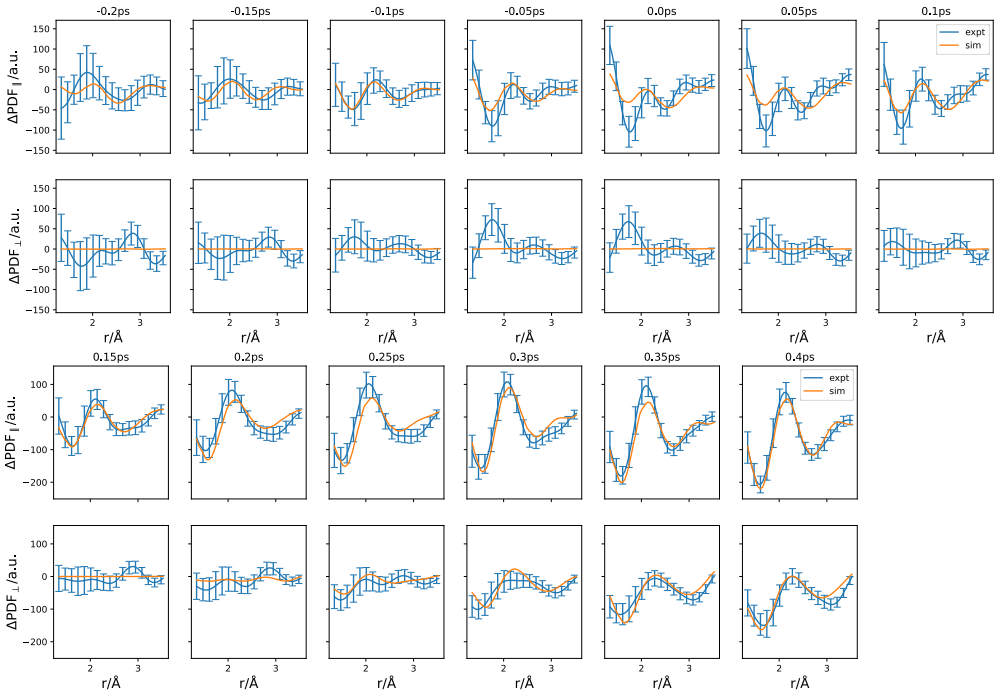

Fig. 1 Genetic fitting results and corresponding experimental data.

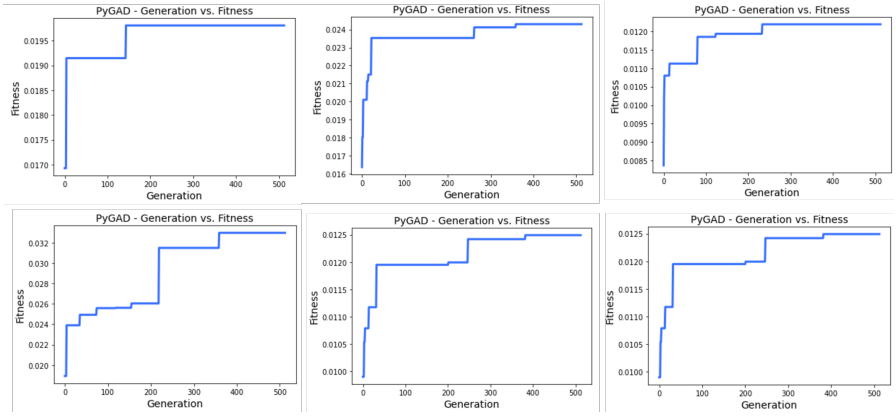

Fig. 2 Fitness and the number of generations across multiple fitting processes.

10 Pump pulse energy scan

We obtained difference diffraction patterns at 9 different pump pulse intensities. In Fig. 3, we show their pump pulse energy-dependent integrated signal intensity in a momentum transfer range between 1.0Å^{-1} and 2.0Å^{-1}. The graph shows a clear linear feature within 140μJ pump pulse energy. For our time-dependent experiments, we kept the pump pulse energy at 30μJ.

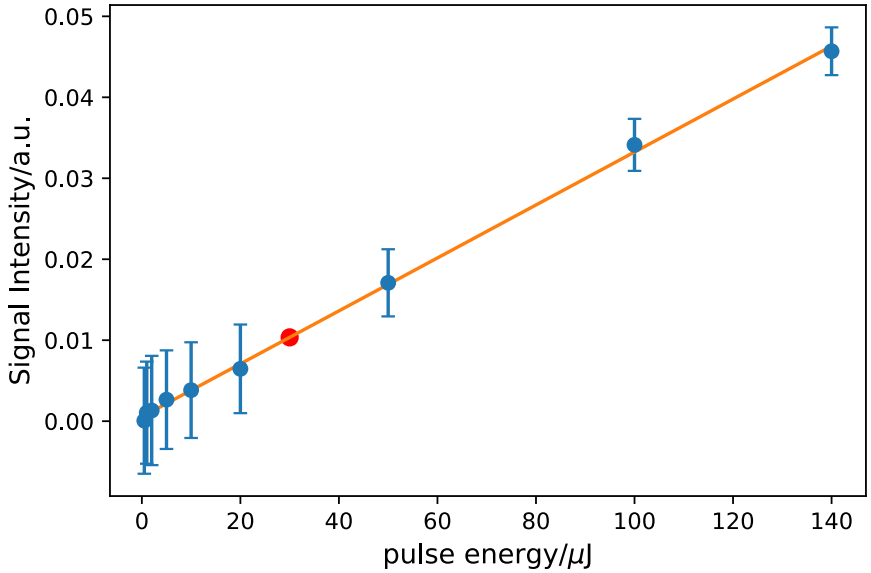

Fig. 3 Results of a pump pulse intensity scan. Error bars represent a 68 % confidence interval obtained from bootstrap analysis. The red dot represents the pump energy used in the experiment.

11 Rotational dephasing simulation of $Fe(CO)_5$

The averaged atom pair orientation $< \cos^2(\Omega(t)) >$ [10] evolution over time at 300K and 50K is shown in Fig.4. Ω represents the angle between the atom pair and laser polarization in a single molecule, and '<>' represents ensemble average. $< \cos^2(\Omega) >= 1$ corresponds to an ideally aligned ensemble with a $\cos^2$ distribution. However, thermal rotational excitation of the molecules in the ensemble causes this coherent alignment to dephase. The dephasing rate depends on the temperature, and the molecules are cooled through supersonic expansion during the sample delivery process. For this analysis, we use approximate upper and lower temperature limits: 300K, representing ambient temperature, and 50K, based on the rotational temperature of N_2 measured using UED[11]. As shown in Fig. 4B, even at the upper temperature limit, anisotropy remains significant until around 0.8ps. However, in Fig.4 of the main text, anisotropy begins to vanish at 0.3 ps. This discrepancy indicates that the loss of anisotropy is primarily due to the molecule's intrinsic distortion rather than rotational dephasing.

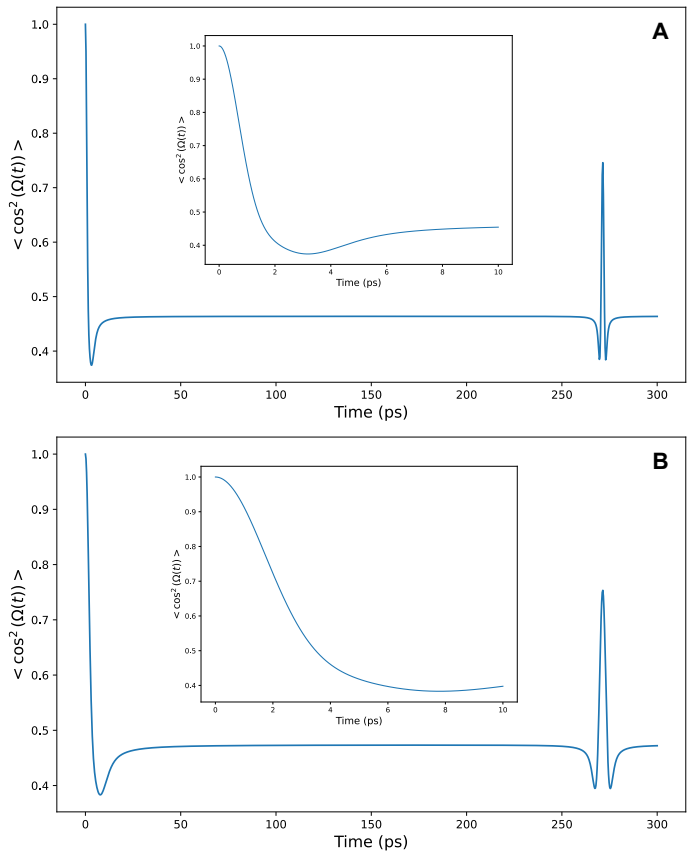

Fig. 4 The simulated averaged atom pair orientation $< \cos^2(\Omega) >$ evolution over time at 300K(A) and 50K(B).The anisotropy remains significant in between 0.3 and 0.8ps(time window of main text's Fig.4) at both temperatures.

12 Comparison of UED and UXS Studies on $Fe(CO)_5$ Photodissociation Dynamics

A recent ultrafast X-ray scattering (UXS) study on this system, using pump light with the same central wavelength, was published on ChemRxiv[12]. However, it arrived at conclusions notably different from those of this study, particularly regarding the absence of a pre-dissociation region. One key experimental distinction between these methods is the upper limit of the detection range in reciprocal space, which is 4.34Å^{-1} in UXS and 10.26Å^{-1} in UED.

Figures 5A and B show the isotropic diffraction intensity difference measured in UXS and UED, respectively. The dashed green lines separate various diffraction peaks observed at long time delays (e.g., 1 ps) within the 4Å^{-1} range. While the absolute intensities of these peaks differ due to the intrinsic nature of the techniques or differences in data analysis processes, the peak positions at long time delays are nearly identical between the two methods, indicating that both are probing the same dynamics in this regime.

However, at short time delays in the UED experiment (corresponding to the pre-dissociation period, -100–250fs, as discussed in this study), no significant signal is observed within the 4.34Å^{-1} range. Instead, the primary signals are located around $6 \sim 9\text{Å}^{-1}$ (highlighted by the dashed black box in Fig.5B), which lies outside the Q range of UXS. Consequently, this particular UXS study cannot effectively resolve the subtle pre-dissociation signals within its Q range. This originates from the nature of diffraction experiments: large bond length changes (such as dissociation) appears in the small q region, while small bond length changes (such as vibration) appears in the large q region.

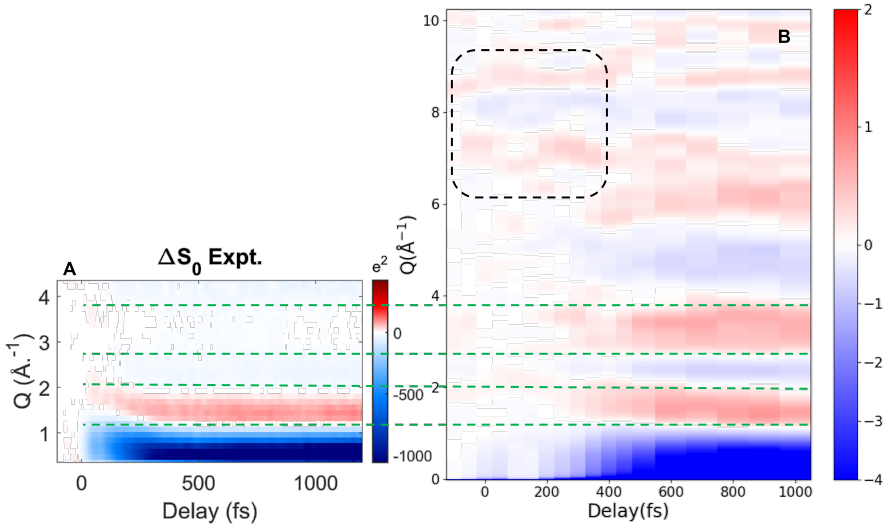

Fig. 5 A, Experimental scattering difference curves for the isotropic scattering component of UXS, directly adapted from Fig. S1 of [12]. B, Isotropic component of the experimental scattering difference in UED ($\beta_0(s,t)$ in Eqn.7). The two graphs are aligned at the positions of 2Å^{-1} and 4Å^{-1}. The dashed green lines mark the boundaries of the UED peaks within the 4Å^{-1} range. The dashed black box highlights the main UED signal observed between -100fs and 250fs.

13 The character of incoherent bond vibration

First, we assume that the bond vibration observed here is a harmonic vibration. According to previous AIMD simulation results[13], the vibration period of the axial Fe–C bond is approximately 70fs. However, the temporal resolution of our experiment is roughly 150fs, which is significantly longer than the vibration period. Thus, we can infer that the observed signal represents incoherent bond vibrations.

To illustrate this, we use the -0.1 ps time point as an example. Fig.6A shows a schematic $\Delta\text{PDF}_{\parallel}$ of the axial Fe–C bond in Fe(CO)_5, vibrating with the same amplitude as at the -0.1 ps time point and with infinitely short temporal resolution. It is evident that the peaks oscillate with a period of 70 fs. Fig. 6B demonstrates the effect of temporal smoothing applied to Fig.6A using a Gaussian kernel with a FWHM of 150 fs to simulate the experimental temporal resolution. The smoothed result does not exhibit any distinct vibrational character but instead displays a weak negative peak around 1.83 Å, flanked by two weak positive peaks.

This feature arises because, in an ensemble of incoherent vibrating molecules, the vibrations reduce the number of bonds exactly at the equilibrium length. This reduction is redistributed to bond lengths slightly longer and shorter than the equilibrium length, resulting in the observed "positive-negative-positive" sandwich-like pattern. This characteristic is also evident in the pre-dissociation process observed in the experiment.

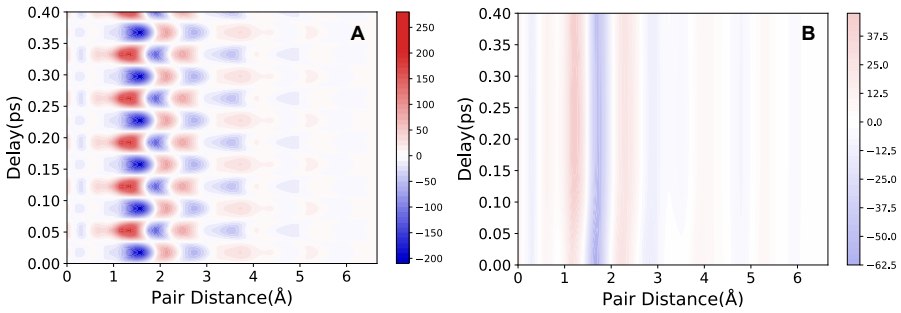

Fig. 6 A, schematic $\Delta PDF_{\parallel}$ of the vibration of axial Fe–C bond in $Fe(CO)_5$, with infinitely short temporal resolution. B, the temporal smooth of A using a Gaussian kernel with a FWHM of 150 fs to simulate the experimental temporal resolution.

Fig.7 compares the smoothed scheme (a slice from Fig.6B), the experimental data at -0.1ps, the corresponding fitting result, and a structure without vibration where the axial Fe–C bond is stretched by 0.05Å. Firstly, the three vibration-based structures show excellent agreement, particularly around 1.83Å. The smoothed scheme slightly differs from the other two, which is due to the equation used for fitting (Eqn. 13) being a first-order approximation of the exact solution (Eqn. 12). However, this level of precision is sufficient to identify the presence of vibrations in the experimental data and to distinguish between strong vibrations and simple bond stretching.

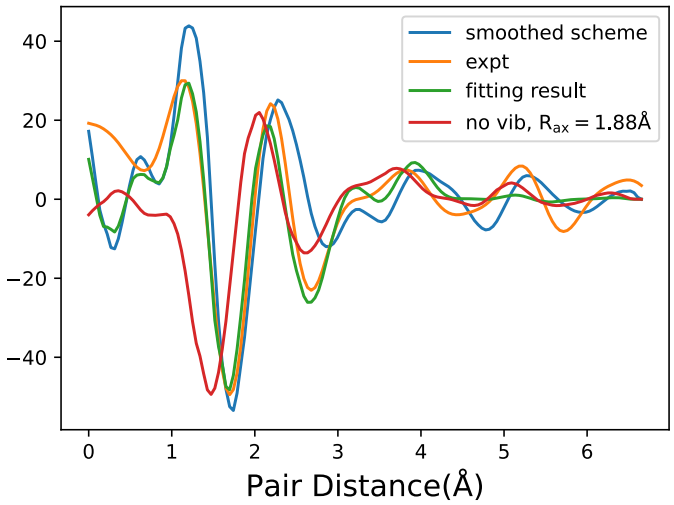

Fig. 7 The $\Delta PDF_{\parallel}$ comparison includes the smoothed scheme (a slice from Fig.6B), the experimental data at -0.1ps, the corresponding fitting result, and a structure without vibration where the axial Fe–C bond is stretched by 0.05Å. The three vibration-based structures exhibit excellent agreement, while the stretched structure shows a significantly different peak position, clearly distinguishing it from the vibration-based features.

References

[1] Wolf, T.J.A., Sanchez, D.M., Yang, J., Parrish, R.M., Nunes, J.P.F., Centurion, M., Coffee, R., Cryan, J.P., Gühr, M., Hegazy, K., Kirrander, A., Li, R.K., Ruddock, J., Shen, X., Vecchione, T., Weathersby, S.P., Weber, P.M., Wilkin, K., Yong, H., Zheng, Q., Wang, X.J., Minitti, M.P., Martínez, T.J.: The photochemical ring-opening of 1,3-cyclohexadiene imaged by ultrafast electron diffraction. Nature Chemistry **11**(6), 504–509 (2019) https://doi.org/10.1038/s41557-019-0252-7

[2] Champenois, E.G., Sanchez, D.M., Yang, J., Nunes, J.P.F., Attar, A., Centurion, M., Forbes, R., Gühr, M., Hegazy, K., Ji, F., Saha, S.K., Liu, Y., Lin, M.-F., Luo, D., Moore, B., Shen, X., Ware, M.R., Wang, X.J., Martínez, T.J., Wolf, T.J.A.: Conformer-specific photochemistry imaged in real space and time. Science **374**(6564), 178–182 (2021) https://doi.org/10.1126/science.abk3132 https://www.science.org/doi/pdf/10.1126/science.abk3132

[3] Salvat, F., Jablonski, A., Powell, C.J.: elsepa—dirac partial-wave calculation of elastic scattering of electrons and positrons by atoms, positive ions and molecules. Computer Physics Communications **165**(2), 157–190 (2005) https://doi.org/10.1016/j.cpc.2004.09.006

[4] Yang, J., Zhu, X., Wolf, T.J.A., Li, Z., Nunes, J.P.F., Coffee, R., Cryan, J.P., Gühr, M., Hegazy, K., Heinz, T.F., Jobe, K., Li, R., Shen, X., Veccione, T., Weathersby, S., Wilkin, K.J., Yoneda, C., Zheng, Q., Martinez, T.J., Centurion, M., Wang, X.: Imaging CF_3I conical intersection and photodissociation dynamics with ultrafast electron diffraction. Science **361**(6397), 64–67 (2018) https://doi.org/10.1126/science.aat0049

[5] Liu, Y., Horton, S.L., Yang, J., Nunes, J.P.F., Shen, X., Wolf, T.J.A., Forbes, R., Cheng, C., Moore, B., Centurion, M., Hegazy, K., Li, R., Lin, M.-F., Stolow, A., Hockett, P., Rozgonyi, T., Marquetand, P., Wang, X., Weinacht, T.: Spectroscopic and structural probing of excited-state molecular dynamics with time-resolved photoelectron spectroscopy and ultrafast electron diffraction. Physical Review X **10**(2), 021016 (2020) https://doi.org/10.1103/PhysRevX.10.021016

[6] Glownia, J.M., Natan, A., Cryan, J.P., Hartsock, R., Kozina, M., Minitti, M.P., Nelson, S., Robinson, J., Sato, T., Driel, T., Welch, G., Weninger, C., Zhu, D., Bucksbaum, P.H.: Self-referenced coherent diffraction x-ray movie of ångstrom- and femtosecond-scale atomic motion. Physical Review Letters **117**, 153003 (2016) https://doi.org/10.1103/PhysRevLett.117.153003

[7] Baskin, J.S., Zewail, A.H.: Ultrafast electron diffraction: Oriented molecular structures in space and time. ChemPhysChem **6**(11), 2261–2276 (2005) https://doi.org/10.1002/cphc.200500331 https://chemistry-europe.onlinelibrary.wiley.com/doi/pdf/10.1002/cphc.200500331

[8] Baskin, J.S., Zewail, A.H.: Oriented ensembles in ultrafast electron diffraction. ChemPhysChem **7**(7), 1562–1574 https://doi.org/10.1002/cphc.200600133 https://chemistry-europe.onlinelibrary.wiley.com/doi/pdf/10.1002/cphc.200600133

[9] Gad, A.F.: Pygad: An intuitive genetic algorithm python library. Multimedia Tools and Applications, 1–14 (2023)

[10] Baskin, J.S., Zewail, A.H.: Ultrafast electron diffraction: Oriented molecular structures in space and time. ChemPhysChem **6**(11), 2261–2276 (2005) https://doi.org/10.1002/cphc.200500331 https://chemistry-europe.onlinelibrary.wiley.com/doi/pdf/10.1002/cphc.200500331

[11] Yang, J., Guehr, M., Vecchione, T., Robinson, M.S., Li, R., Hartmann, N., Shen, X., Coffee, R., Corbett, J., Fry, A., Gaffney, K., Gorkhover, T., Hast, C., Jobe, K., Makasyuk, I., Reid, A., Robinson, J., Vetter, S., Wang, F., Weathersby, S., Yoneda, C., Centurion, M., Wang, X.: Diffractive imaging of a rotational wavepacket in nitrogen molecules with femtosecond megaelectronvolt electron pulses. Nature Communications **7**(1), 11232 (2016) https://doi.org/10.1038/ncomms11232

[12] Schori, A., Biasin, E., Banerjee, A., Boutet, S., H. Bucksbaum, P., Carbajo, S., J. Gaffney, K., Glownia, J., Hartsock, R., Ledbetter, K., Kaldun, A., Koglin, J.E., Kunnus, K., Lane, T.J., Liang, M., Minitti, M.P., O'Neal, J.T., Parrish, R.M., Poitevin, F., Ruddock, J.M., Nelson, S., Stankus, B., Weber, P.M., Wolf, T.J.A., Odelius, M., Natan, A.: Real-space Observation of a Transition Metal Complex Dissociation and Energy Redistribution. https://chemrxiv.org/engage/chemrxiv/article-details/66cec719a4e53c4876db4de6

[13] Banerjee, A., Coates, M.R., Kowalewski, M., Wikmark, H., Jay, R.M., Wernet, P., Odelius, M.: Photoinduced bond oscillations in ironpentacarbonyl give delayed synchronous bursts of carbonmonoxide release. Nature Communications **13**(1), 1337 (2022) https://doi.org/10.1038/s41467-022-28997-z